PASJ: Publ. Astron. Soc. Japan **52**, 803–820 (2000)

CO Observations of Luminous IR Galaxies at Intermediate Redshift

Yoshinori TUTUI,[1*] Yoshiaki SOFUE,[1] Mareki HONMA,[2,3] Takashi ICHIKAWA,[4] and Ken-ichi WAKAMATSU[5]

[1]*Institute of Astronomy, The University of Tokyo, Mitaka, Tokyo 181-8588*
E-mail (YT): tutui@sci.nhk.or.jp
[2]*VERA Project Office, National Astronomical Observatory, Mitaka, Tokyo 181-8588*
[3]*Mizusawa Astrogeodynamics Observatory, National Astronomical Observatory, Mizusawa, Iwate 023-0861*
[4]*Astronomical Institute, Tohoku University, Aoba, Sendai 980-8578*
[5]*Department of Technology, Gifu University, 1-1 Yanagido, Gifu 501-1193*

(Received 1999 December 3; accepted 2000 June 5)

Abstract

We present new measurements of the ^{12}CO ($J = 1$–0) emission from 16 luminous infrared galaxies (LIGs) at intermediate redshift ($cz \sim 10000$–50000 km s^{-1}). These new data were selected by isolated and normal morphology. Although there already exist measurements of CO emission from LIGs in the literature, they are mostly strongly interacting/merging systems. The new CO data represent an important new addition to the literature in that they both expand the relatively small number of samples of LIGs measured in CO, and they include an interesting subset of LIGs that were selected based on isolated and normal morphology. The CO observations were performed using the NRO 45-m telescope. From measurements of the CO emission and the IRAS database, we discuss the molecular gas and dust properties of late-type galaxies at intermediate redshift. Comparisons of the CO and dust properties of the new result with those from other CO measurements have revealed the characteristics of this sample: (1) It shows the deepest CO observations of IRAS galaxies at intermediate redshift without any strong interaction features. (2) It has typical properties of normal IRAS galaxies in terms of star-formation efficiency, color–color diagrams and galactic nuclear activity. (3) It has a smaller gas-to-dust ratio than normal IRAS galaxies. This can be explained by a two-component dust model; our sample consists of mostly warm dust.

Key words: galaxies: distances and redshifts — galaxies: ISM — galaxies: spiral

1. Introduction

The Infrared Astronomical Satellite (IRAS) has revealed a number of extragalactic objects with luminosity dominated by FIR emission (e.g., Soifer et al. 1984). IRAS has surveyed 96% of the sky, with a completeness limit of ~ 0.5 Jy at 12 μm, 25 μm, and 60 μm, and ~ 1.5 Jy at 100 μm, and with an angular resolution of $\sim 0'.5$ for 12 μm and $\sim 2'$ for 100 μm. It discovered ~ 20000 galaxies, which had not been previously cataloged. The majority of IRAS extragalactic galaxies are late-type galaxies. Galaxies detected by IRAS, whose luminosity is dominated by FIR emission, are called IRAS galaxies, and are categorized as luminous infrared galaxies (LIGs) with infrared luminosities of $L_{\rm IR} > 10^{11}\,L_\odot$, ultraluminous infrared galaxies (ULIGs) for $L_{\rm IR} > 10^{12}\,L_\odot$, and hyperluminous infrared galaxies (HyLIGs) for $L_{\rm IR} > 10^{13}\,L_\odot$. Infrared luminous galaxies, whose luminosity is more than $10^{11}\,L_\odot$, become the dominant population at an intermediate redshift of $z \lesssim 0.3$ (Sanders, Mirabel 1996). The fraction of merger and interacting systems among IRAS galaxies increases with the infrared luminosity; that is $\sim 12\%$ for $\log(L_{\rm IR}/L_\odot) = 10.5$–11, $\sim 32\%$ for $\log(L_{\rm IR}/L_\odot) =$ 11–11.5, $\sim 66\%$ for $\log(L_{\rm IR}/L_\odot) = 11.5$–12, and $\sim 95\%$ for $\log(L_{\rm IR}/L_\odot) > 12$ (Sanders, Mirabel 1996).

CO-line observations have revealed that LIGs are extremely rich in molecular gas. Early CO observations of infrared selected galaxies with $L_{\rm IR} = 10^{10}$–$10^{11}\,L_\odot$ showed a rough correlation between the CO and FIR luminosity (Young et al. 1984, 1986). A number of single-dish CO surveys of IRAS galaxies have been performed (Sanders et al. 1991; Mirabel et al. 1990; Tinney et al. 1990; Downes et al. 1993; Mazzarella et al. 1993; Young et al. 1995; Elfhag et al. 1996; Solomon et al. 1997), which consist of galaxies with IR luminosities of $L_{\rm IR} = 10^{10}$–$10^{13}\,L_\odot$ from nearby to intermediate redshift. Correlations between CO and IR luminosities are also

* Present address: NHK (Japan Broadcasting Corporation), Program Production Department, Science Programs Division, 2-2-1 Jinnan, Shibuya-ku, Tokyo 150-8001.

found for these samples. Furthermore, it is found that the IR-to-CO luminosity ratio ($L_{\rm IR}/L'_{\rm CO}$), which represents the star-formation efficiency in a galaxy, increases with the CO luminosity, suggesting that molecular-gas-rich galaxies show a high star-forming efficiency. Assuming a galactic ^{12}CO (J = 1–0)–H_2 conversion factor of $N_{\rm H_2}/I_{\rm CO} = 3.0 \times 10^{20}$ the total molecular-gas mass for ULIGs is as high as $M_{\rm H_2} \gtrsim 10^{10}\,M_\odot$, and the star-formation efficiency in ULIGs is, on average, much higher than any of the most active star-forming galactic GMC cores.

CO observations of ULIGs at intermediate redshift ($cz \sim$ 10000–50000 km s^{-1}) have been performed by Mirabel et al. (1990) using the SEST 15-m telescope, Sanders et al. (1991) using the NRAO 12-m telescope, Solomon et al. (1997) using the IRAM 30-m telescope, and Lavezzi and Dickey (1998) using the NRAO 12-m telescope (see Sanders, Mirabel 1996, for more references). In addition to the above, we have performed CO observations using the NRO 45-m telescope. CO observations for ULIGs at intermediate redshift are important concerning the following points: (1) Objects at intermediate redshift ($z \sim$ 0.1–1) are significant for galactic evolution from the most-active epoch at $z \sim$ 1–2, to the local Universe at $z \sim 0$. (2) Galaxies at intermediate redshift are the most distant targets in which we can detect the CO-line from the galactic disk, which is related to the global properties of the molecular gas in a galaxy. (3) A high ratio of merger or interacting systems and a high star-formation efficiency of ULIGs can help reveal the star-formation history. (4) Strong CO emission and stable CO linewidths can be used for the Tully–Fisher relation to measure the distances to galaxies at intermediate redshift. Photometric observations for the CO-line Tully–Fisher relation have been performed using the Okayama Astrophysical Observatory 1.88-m telescope, and the results will be discussed in a forthcoming paper.

The results of our CO-line observations and definitions of CO and FIR properties discussed in this paper are described in section 2. We compare our sample with these CO observations to evaluate the characteristics of our sample in section 3. The results are discussed in section 4, and summarized in section 5. We also discuss the samples in terms of the IRAS color–color diagrams and galactic activities in appendices 1 and 2. Throughout this paper we use $H_0 = 75$ km s^{-1} Mpc^{-1} and $q_0 = 0.5$.

2. Data and CO Observations

^{12}CO (J = 1–0) line observations of galaxies at intermediate redshift were obtained using the Nobeyama Radio Observatory (NRO) 45-m telescope. We also use data from the literature (Solomon et al. 1997; Sanders et al. 1991; Mirabel et al. 1990; Lavezzi, Dickey 1998). In comparing these samples, we used given integrated intensities and the same formulae to estimate the CO luminosities, or molecular gas mass.

2.1. Sample Selection

The main purpose of our CO observations was to obtain CO linewidths in order to apply them to the CO-line Tully–Fisher relation to measure the distances to galaxies and to determine the Hubble constant at intermediate redshift. The target was late-type galaxies with bright CO-line emission and isolated normal morphology located at intermediate redshift. The sample selection was made using the following criteria.

(1) *Redshift criterion.* The redshift criterion of the sample was cz = 10000–20000 km s^{-1} in 1994/1995 observations and cz = 20000–30000 km s^{-1} in 1995/1996 observations. After we confirmed the possibility of CO detection at such redshifts, we set the redshift criterion to cz = 30000–50000 km s^{-1} in 1996/1997 observations.

(2) *FIR flux density criterion.* In order to obtain sufficient CO emission at intermediate redshift we selected relatively strong FIR-emission sources at 60 μm and 100 μm, because FIR emission, which is dominated by the thermal emission of dust heated by surrounding starlight in UV, is related to CO emission from dense molecular-gas regions. We selected galaxies whose IRAS flux densities at 60 μm and 100 μm are greater than 1 Jy.

(3) *Morphology criterion.* Although morphology information at intermediate redshift was not sufficient in catalogs, we judged the morphology of the sample using images from the STScI Digitized Sky Survey (DSS). Strong interacting galaxies and mergers were excluded from the sample. However, weakly interacting galaxies, whose tails or irregular arms were not resolved by the DSS images at the resolution limit of $\sim 1''$, were included, because the influences of weak interaction do not affect the CO line-width very much compared to the H I linewidth (Tutui, Sofue 1997).

(4) *Position error criterion.* Since the half-power beam width (HPBW) of the NRO 45-m telescope was 15″ at the frequency of ^{12}CO (J = 1–0), 115.271204 GHz in the object rest frame, galaxies whose position error listed in the NASA Extragalactic Database (NED) is less than 10″ were selected. We also cross-checked the position using the DSS images.

(5) *Recession velocity error criterion.* The band width of the ^{12}CO (J = 1–0) observation of the NRO 45-m telescope was 250 MHz, corresponding to 650 $(1+z)$ km s^{-1}. Since the linewidths of the observed galaxies were expected to be about 200–500 km s^{-1}, the recession velocity error criterion to select galaxies was less than 100 km s^{-1}. The recession velocity was taken from the IRAS redshift surveys by Strauss et al. (1992) and Fisher et al. (1995).

Table 1. Galaxies detected in the CO-line using the NRO 45-m telescope.

Galaxy	RA(B1950) h m s	Dec(B1950) ° ′ ″	cz km s^{-1}	z	D_L Mpc	Type
PG 0157+001	01 57 16.3	+00 09 09	48869	0.16301	676.64	—
IRAS 02185+0642	02 18 40.3	+06 43 03	29347	0.09789	400.70	—
IRAS 02411+0354‡	02 41 09.3	+03 53 56	43050	0.14360	593.66	—
IRAS 07243+1215†	07 24 20.6	+12 15 09	28204	0.09408	384.77	—
I Zw 23	09 56 01.0	+52 29 48	12224	0.04077	164.73	S?
CGCG 1113.7+2936	11 13 47.1	+29 35 58	13880	0.04630	187.29	SB(s)b
IC 2846	11 25 24.8	+11 26 01	12294	0.04101	165.68	—
IRAS 14060+2919	14 06 04.9	+29 18 59	35060	0.11695	480.72	—
CGCG 1417.2+4759	14 17 14.8	+47 59 00	21465	0.07160	291.35	—
IRAS 14210+4829†	14 21 06.2	+48 29 59	22690	0.07569	308.26	—
CGCG 1448.9+1654	14 48 54.5	+16 54 02	13700	0.04570	184.84	—
NGC 6007	15 51 01.6	+12 06 27	10547	0.03518	141.94	SABbc:
IRAS 16533+6216	16 53 19.8	+62 16 36	31808	0.10610	435.10	—
PGC 60451	17 30 00.6	+20 09 49	14989	0.05000	202.43	—
IRAS 17517+6422	17 51 45.0	+64 22 14	26151	0.08723	356.22	—
IRAS 23389+0300	23 38 56.9	+03 00 48	43470	0.14500	599.63	—

Col.(1): Galaxy name. A dagger and double dagger denote a galaxy of marginal detection and upper limit of the detection, respectively. Col.(2) and (3): Coordinates in B1950. Col.(4): Heliocentric velocity. Col.(5): Heliocentric redshift from Fisher et al. (1995). Col.(6): Luminosity distance derived from the redshift in Col.(5). Col.(7): Morphological type from RC3 (de Vaucouleurs et al. 1991).

2.2. *CO Observations*

CO-line observations were performed as a NRO 45-m long-term project, and were carried out on January 14 to 23 and December 9 to 12 in 1994, January 6 to 10, March 13 to 17, and December 17, 18, 21, 22 in 1995, January 17 to 22, February 18 to 22, and December 2 to 5 in 1996, and January 8 to 12 in 1997. The HPBW of the NRO 45-m telescope was 15″ at the frequency of ^{12}CO (J = 1–0) line, and the aperture and main-beam efficiencies were η_a = 0.35 and η_{mb} = 0.50, respectively, as measured by observing the planets Mars and Saturn. As the receiver front-ends, we used cooled SIS (superconductor-insulator-superconductor) receivers, which could receive two orthogonal polarizations simultaneously, with an SSB filter to select one of the sidebands. The receiver back-ends were 2048-channel wide-band acousto-optical spectrometers (AOS). The total channel number corresponds to frequency widths of 250 MHz and, therefore, to a velocity coverage in the rest frame of the galaxy of $\sim$ 650 km s^{-1}. The center frequency was set to the 1024-channel, which corresponded to 115.271204 $(1+z)^{-1}$ GHz for each galaxy. The system noise temperature was 300–800 K in the single side band at the observing frequencies. Calibration of the line intensity was made using an absorbing chopper in front of the receiver, yielding an antenna temperature (T_A^*), corrected for both the atmospheric and antenna ohmic losses. The intensity scale of T_A^* was converted to the main-beam brightness temperature by $T_{mb} = T_A^*/\eta_{mb}$. Subtraction of sky emission was performed by on–off position switching, and the offset of the off-position was 5′ away from the on-position. The on-source total integration time for each galaxy ranged from 30 min to 3 hr. Antenna pointing was performed by observing nearby SiO maser sources at 43 GHz every 60–90 min. The pointing accuracy was better than ±4″ during all observations. The total observation time for the on/off position integrations and pointing was about 90 min to 9 hr for individual galaxies. After flagging bad spectra, subtraction of the baseline was performed by linear-baseline fitting. Adjacent channels were binned to a velocity resolution of 10 km s^{-1}. The noise level of the resultant spectra at a velocity resolution of 10 km s^{-1} was 2–5 mK in T_A^*.

2.3. *CO-Line Profiles*

We have obtained CO-line spectra of sixteen galaxies at intermediate redshifts, $cz \sim$ 10000–50000 km s^{-1}, which are listed in table 1. These galaxies are some of the most distant examples of IRAS galaxies whose CO-line has been detected. The observed CO-line profiles are shown in figure 1. Measurements of the CO integrated intensities and linewidths were carefully performed, not only by using the final CO-line profiles, but also by comparing the CO-line profiles between individual spectrometers and each run. In table 2 we list the observed prop-

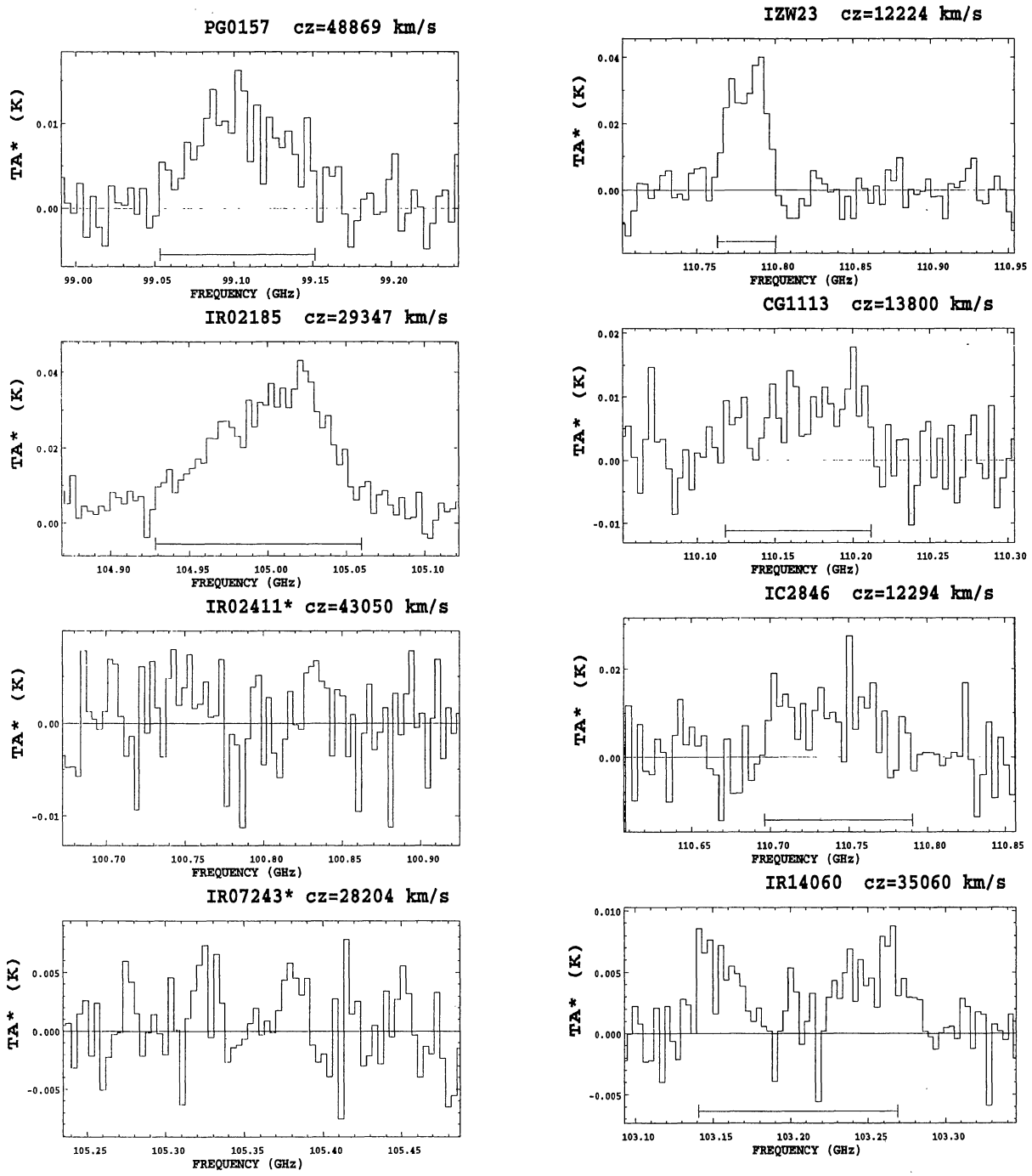

Fig. 1. CO-line profiles for all galaxies whose CO linewidth was obtained using the NRO 45-m telescope. The scale of intensity is the antenna temperature ($T_{\rm A}^{*}$). The center of the abscissa is the heliocentric radial velocity/frequency given by optical redshift determinations.

erties of the CO-line profiles; the on-source integration time, the r.m.s. antenna temperature, the CO linewidths at the observed and rest frames, the antenna temperature at the peak level, and the integrated intensity corrected for the main beam efficiency.

2.4. CO Luminosities and Molecular Gas Properties

The CO luminosity is expressed mainly in two ways. One is formulated by an integrated flux density with a unit of $L_{\odot}$. The other is formulated by the integrated intensity, or sometimes the integrated flux density, with

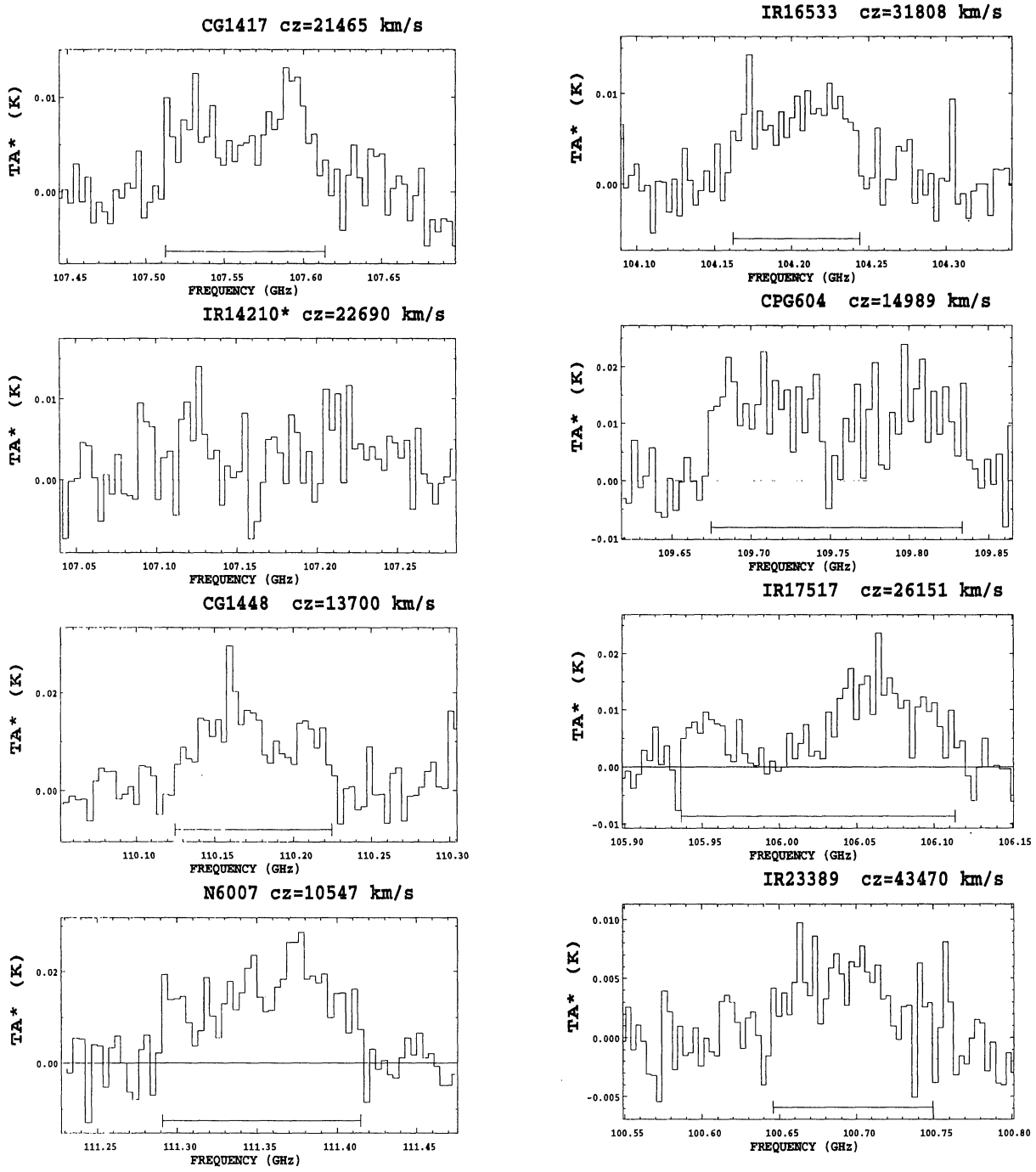

Fig. 1. (Continued)

units of K km s^{-1} pc^2. The observed integrated intensity is described by

$$I_{\nu_{\rm obs}} = \int T_{\rm mb} dV_{\rm obs}, \quad (1)$$

where $T_{\rm mb}$ is the main beam temperature related to the antenna temperature, $T_{\rm A}^*$, and the main beam efficiency, $\eta_{\rm mb}$, as $T_{\rm mb} = T_{\rm A}^*/\eta_{\rm mb}$. We should note the integrated intensity for a point source object when comparing between different measurements, because the intensity depends on the beamsize and efficiencies. For example, the observed integrated intensity of PG 0157 (= Mrk 1014), which should essentially be a point source for both the NRO 45-m and IRAM 30-m telescopes, are 5.11 K km s^{-1} for

Table 2. CO-line observation results using the NRO 45-m telescope.

Galaxy	cz km s^{-1}	$t_{\rm int}$ min	r.m.s. mK	$W_{\rm obs}$ km s^{-1}	$W_{\rm rest}$ km s^{-1}	$T_{\rm A}^{*}$ mK	$I_{\rm CO}$ K km s^{-1}	
PG 0157+001	48869	90	2	349	300	15	5.11	(0.22)
IRAS 02185+0642	29347	90	4	391	356	40	13.05	(0.48)
IRAS 02411+0354‡	43050	60	5	498	435	8	<1.90	(0.66)
IRAS 07243+1215†	28204	90	3	237	217	6	1.79	(0.28)
I Zw 23	12224	60	4	108	104	39	4.82	(0.26)
CGCG 1113.7+2936	13880	60	5	313	299	14	4.33	(0.55)
IC 2846	12294	30	4	374	360	19	4.78	(0.48)
IRAS 14060+2919	35060	120	3	420	376	8	1.91	(0.37)
CGCG 1417.2+4759	21465	180	3	314	293	13	4.66	(0.32)
IRAS 14210+4829†	22690	60	4	496	461	11	3.08	(0.54)
CGCG 1448.9+1654	13700	60	4	295	282	28	7.03	(0.42)
NGC 6007	10547	60	7	360	347	28	11.24	(0.82)
IRAS 16533+6216	31808	90	3	236	213	10	3.54	(0.28)
PGC 60451	14989	60	7	482	459	20	10.35	(0.95)
IRAS 17517+6422	26151	90	5	522	480	19	4.00	(0.69)
IRAS 23389+0300	43470	180	3	311	272	8	3.92	(0.31)

Col.(1): Galaxy name. A dagger and double dagger denote a galaxy of marginal detection and upper limit of the detection, respectively. Col.(2): Redshift in cz. Col.(3): Integration time of on-source in minute. Col.(4): Root mean square of antenna temperature after binning of 10 km s^{-1} in emission-free region of the spectrum. Col.(5): Observed CO linewidth defined as the full width at 20% of the maximum intensity. Col.(6): CO linewidth converted to the rest frame. Col.(7): Antenna temperature at the peak level intensity. Col.(8): Integrated intensity corrected for the main beam efficiency. Col.(9): Uncertainty of $1\,\sigma$ in the integrated intensity.

NRO 45-m and 1.8 K km s^{-1} for IRAM 30-m in Solomon et al. (1997), but are consistent within 50% of the integrated intensity for the efficiency of $\eta_{\rm a} = 0.35$ and $\eta_{\rm mb} = 0.5$ for the NRO 45-m, and $\eta_{\rm a} = 0.3$ and $\eta_{\rm mb} = 0.6$ for the IRAM 30-m.

The CO luminosity, $L'_{\rm CO}$, in units of K km s^{-1} pc^2 is denoted by the observed integrated intensity, $I_{\nu_{\rm obs}}$, and the beam solid angle, $\Omega_{\rm b}$, as

$$L'_{\rm CO} = \frac{\Omega_{\rm b} I_{\nu_{\rm obs}} D_{\rm L}^2}{(1+z)^3}, \tag{2}$$

where z is the redshift and $D_{\rm L}$ is the luminosity distance formulated using the Hubble constant, H_0, and the deceleration parameter, q_0, as

$$D_{\rm L} = \frac{c}{H_0 q_0^2}\left[q_0 z + (q_0 - 1)(\sqrt{2q_0 z + 1} - 1)\right]. \tag{3}$$

The mass of the molecular gas is estimated from CO emission, assuming the galactic CO-to-H_2 conversion factor. We adopt a conversion factor of $N_{\rm H_2}/I_{\rm CO} = 3.0 \times 10^{20}$ cm^{-2} (K km s^{-1})$^{-1}$ (Strong et al. 1988; Solomon, Barrett 1991). The correction factor from H_2 mass, to molecular gas mass including He and other elements, is referred from Allen (1973), as

$$M_{\rm gas} = 1.36 \times M_{\rm H_2}. \tag{4}$$

We estimated the CO properties of the galaxies based on the results of the CO observations listed in table 3. The ranges of the CO luminosity and molecular gas mass of our sample are $L'_{\rm CO} = 5.5 \times 10^8$–$7.4 \times 10^9\,L_\odot$ and $M_{\rm gas} = 3.3 \times 10^9$–$4.6 \times 10^{10}\,M_\odot$, respectively. These are about 20-times greater than the CO luminosity and the molecular gas mass of the Milky Way, interior to the solar circle (Solomon, Rivolo 1989).

2.5. *FIR Luminosities and Dust Properties*

The FIR luminosities of LIGs are normally adopted by the formula using the IRAS 60 and 100 μm flux densities,

$$\left(\frac{L_{\rm FIR}}{L_\odot}\right) = 3.92 \times 10^5 \times \left[2.58\left(\frac{S_{60}}{\rm Jy}\right) + \left(\frac{S_{100}}{\rm Jy}\right)\right] C \left(\frac{D_{\rm L}}{\rm Mpc}\right)^2, \tag{5}$$

where the constant C is a correction factor of the flux density beyond the range of 60–100 μm, which is typically in the range of 1.5–2.1 (Solomon et al. 1997); here, we assumed $C = 1.8$.

The dust mass is estimated by the dust temperature, $T_{\rm d}$, derived from flux densities at 60 μm and 100 μm of the blackbody radiation. Assuming that the dust emis-

Table 3. CO properties of the observed sample.

Galaxy	I_{CO} K km s^{-1}	$\log L'_{CO}$ K km s^{-1} pc^2	$\log M_{H_2}$ $M_\odot$	$\log(L_{FIR}/L'_{CO})$
PG 0157+001	5.11	9.85	10.50	2.56
IRAS 02185+0642	13.05	9.87	10.53	1.93
IRAS 02411+0354‡	<1.90	<9.33	<9.98	>2.81
IRAS 07243+1215†	1.79	8.98	9.63	2.48
I Zw 23	4.82	8.74	9.39	2.07
CGCG 1113.7+2936	4.33	8.80	9.45	2.16
IC 2846	4.78	8.74	9.39	2.79
IRAS 14060+2919	1.91	9.17	9.83	2.86
CGCG 1417.2+4759	4.66	9.18	9.84	2.10
IRAS 14210+4829†	3.08	9.05	9.70	2.05
CGCG 1448.9+1654	7.03	9.00	9.65	2.08
NGC 6007	11.24	8.98	9.64	1.76
IRAS 16533+6216	3.54	9.37	10.02	2.56
PGC 60451	10.35	9.24	9.89	1.64
IRAS 17517+6422	4.00	9.27	9.92	2.64
IRAS 23389+0300	3.92	9.65	10.30	2.39

Col.(1): Galaxy name. A dagger and double dagger denote a galaxy of marginal detection and upper limit of the detection, respectively. Col.(2): CO integrated intensity. Col.(3): CO luminosity in K km s^{-1} pc^2. Col.(4): Molecular hydrogen gas mass derived with the CO-to-H_2 conversion factor $N(H_2)/I_{CO} = 3.0 \times 10^{20}$ cm^{-2} (K km s^{-1})$^{-1}$, corresponding to $\alpha \equiv M_{H_2}/L_{CO} = 4.5\,M_\odot$ pc^{-2} (K km s^{-1})$^{-1}$. Col.(5): Flux ratio of FIR-to-CO luminosity.

sion follows the emissivity law, $S_\nu \propto \lambda^{-1}$, the dust mass, M_{dust}, is approximately expressed as (Hildebrand 1983)

$$M_{dust} = 4.589 \left(\frac{S_{100}}{\mathrm{Jy}}\right)\left(\frac{D_L}{\mathrm{Mpc}}\right)^2 [\exp(144/T_d) - 1], \quad (6)$$

where, T_d is given by

$$\frac{S_{60}}{S_{100}} = 7.72\,\frac{\exp(144/T_d) - 1}{\exp(240/T_d) - 1}. \quad (7)$$

The ranges of the FIR luminosity and the dust mass of our sample are $L_{FIR} = 5.5 \times 10^{10}$–$2.57 \times 10^{12}\,L_\odot$ and $M_{dust} = 1.7 \times 10^7$–$1.1 \times 10^8\,M_\odot$, respectively. The dust properties of our sample are listed in table 4.

3. Comparison with Other CO-Line Samples

3.1. *Individual CO-Line Samples*

We compared our results (hereafter NRO sample) with other CO-line observations which had been obtained for a number of IRAS galaxies at intermediate redshift. We used data concerning the following four CO samples for a comparison. Hereafter the samples are denoted as the IRAM sample (Solomon et al. 1997), the NRAO-S sample (Sanders et al. 1991), the SEST sample (Mirabel et al. 1990), and the NRAO-L sample (Lavezzi, Dickey 1998). Sampling of IRAS galaxies at intermediate redshift is based on the FIR flux density, because it is generally correlated with the CO flux density. Figures 2 and 3 show plots of the redshift cz against the FIR luminosity and against the CO luminosity for all samples, respectively. The majority of galaxies in the IRAM sample are ULIGs with a higher CO luminosity at a greater intermediate redshift, and are interacting galaxies or mergers. The NRAO-S sample and the SEST sample made pioneering surveys of LIGs in the northern and southern skies, respectively, and were relatively shallower samples. The NRAO-L sample was a sample of IRAS galaxies in clusters of galaxies at relatively lower cz. Our NRO sample shows the deepest CO observations at intermediate redshift. The purpose of our observations was to obtain the CO linewidths of isolated galaxies with normal morphology at intermediate redshift in order to apply them to the CO Tully–Fisher relation. Although the CO emission of normal galaxies is generally not as bright as that for ULIGs, deep observations with long integration have obtained CO emission from galaxies at intermediate redshift. Since the purposes of individual CO observations were different, the properties of the target galaxies in each sample also show various features. Remarks and details concerning individual samples are as follows and are also listed in table 5.

3.2. *CO and FIR Luminosities*

A correlation between the CO and FIR luminosities for LIGs was found by airborne FIR observations (Rickard, Harvey 1984), and by IRAS observations (Young et al.

Table 4. IRAS flux densities and dust properties.

Galaxy	S_{12} Jy	S_{25} Jy	S_{60} Jy	S_{100} Jy	S_{25}/S_{60}	S_{60}/S_{100}	T_d K	log M_{dust} $M_\odot$	log L_{FIR} $L_\odot$
PG 0157+001	0.123	0.542	2.22	2.16	0.244	1.028	48.9	7.91	12.41
IRAS 02185+0642	<0.100	0.212	1.21	2.45	0.175	0.494	35.3	8.02	11.80
IRAS 02411+0354†	<0.085	0.224	1.37	1.95	0.164	0.703	40.6	8.03	12.14
IRAS 07243+1215†	<0.250	<0.545	0.69	0.94	<0.790	0.734	41.4	7.30	11.46
I Zw 23	<0.103	<0.154	0.61	1.74	<0.252	0.351	31.3	7.33	10.81
CGCG 1113.7+2936	<0.088	<0.185	0.63	2.03	<0.294	0.310	30.1	7.59	10.96
IC 2846	<0.173	0.383	4.21	6.72	0.091	0.626	38.7	7.53	11.53
IRAS 14060+2919	<0.096	0.144	1.61	2.42	0.089	0.665	39.7	7.97	12.03
CGCG 1417.2+4759	<0.098	<0.091	0.62	1.54	<0.147	0.403	32.8	7.68	11.28
IRAS 14210+4829†	<0.083	<0.072	0.38	0.88	<0.189	0.432	33.6	7.44	11.10
CGCG 1448.9+1654	<0.079	0.148	1.13	2.09	0.131	0.541	36.5	7.22	11.08
NGC 6007	<0.105	0.123	0.69	2.03	0.178	0.340	31.0	7.29	10.74
IRAS 16533+6216	<0.059	0.169	1.48	2.50	0.358	0.592	37.8	7.98	11.93
PGC 60451	<0.069	<0.088	0.48	1.36	<0.183	0.353	31.4	7.39	10.88
IRAS 17517+6422	0.060	0.149	2.22	3.26	0.067	0.681	40.1	7.83	11.91
IRAS 23389+0300	<0.093	<0.349	1.23	1.17	<0.283	1.051	49.5	7.52	12.04

Col.(1): Galaxy name. Col.(2)–(5): IRAS flux densities at 12, 25, 60, and 100 μm taken from the IRAS Faint Source Catalog (as listed in NED). Col.(6) and (7): IRAS flux ratios. Col.(8): Dust temperature. Col.(9): Dust mass. Col.(10): FIR luminosity.

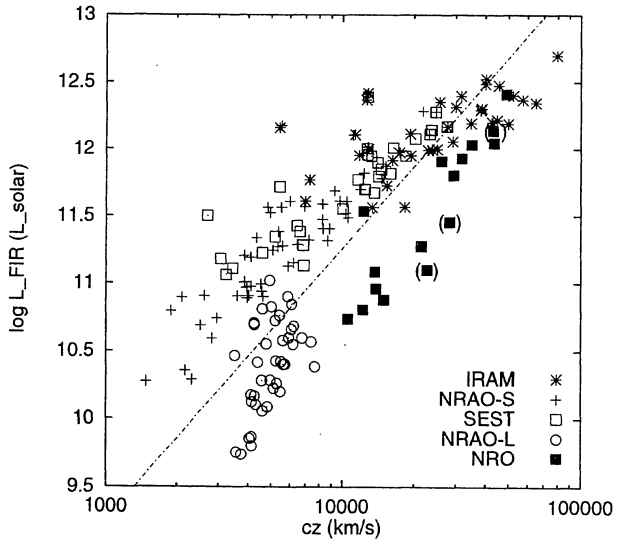

Fig. 2. Redshift (cz) and FIR luminosity (L_{FIR}) distributions for all the samples. IRAM sample (asterisk), NRAO-S sample (plus), SEST sample (open square), NRAO-L sample (open circle), and NRO sample (filled square). The broken line represents an iso-flux line for a source.

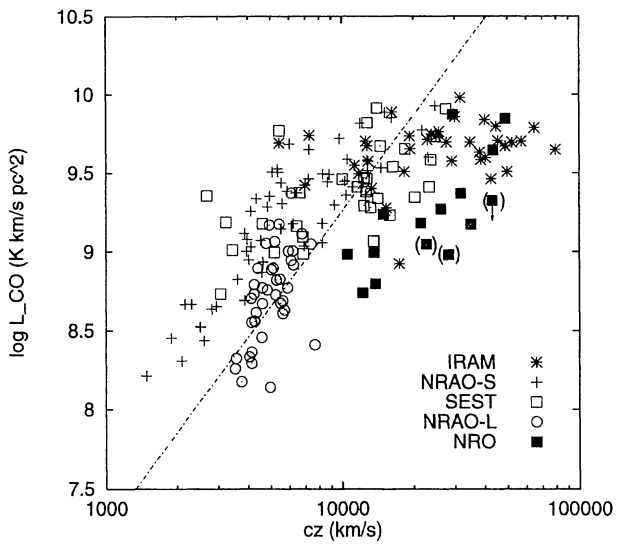

Fig. 3. Redshift (cz) and CO luminosity (L'_{CO}) distributions for all the samples. The symbols are the same as in figure 2. The symbol in parentheses denotes the marginal detection, and the symbol with an arrow denotes the upper/lower limit. The broken line represents an iso-flux line of a source.

1984; Sanders, Mirabel 1985). Figure 4 is a plot of the CO luminosity against the FIR luminosity for all the samples, showing a correlation between the CO and FIR luminosities. The ratio L_{FIR}/L'_{CO}, or L_{FIR}/M_{H_2}, represents the star-formation efficiency (SFE). The correlation shows that SFE for LIGs is higher than that for nearby normal spiral galaxies. Nearby samples presented by Sage (1993) and Solomon and Sage (1988) are indi-

Table 5. Samples of CO observations at intermediate redshift.

Sample name	Reference	Telescope	HPBW $''$	Number	cz km s^{-1}	$\log L_{\rm FIR}$ $L_\odot$
IRAM sample[a]	Solomon et al. (1997)	IRAM 30-m	30	37	10000–60000	11.5–12.5
NRAO-S sample[b]	Sanders et al. (1991)	NRAO 12-m	55	58	3000–25000	10.5–12.0
SEST sample[c]	Mirabel et al. (1990)	SEST 15-m	44	31	5000–25000	11.0–12.5
NRAO-L sample[d]	Lavezzi and Dickey (1998)	NRAO 12-m	55	40	3500–8000	9.0–10.5
NRO sample[e]	This work	NRO 45-m	15	16	10000–50000	11.0–12.0

Col.(1): Sample name used in the text. Remarks and the reference of the samples are mentioned below. Col.(2): Reference which presents the data. Col.(3): Used telescope. Col.(4): The half power beam width of the antenna. Col.(5): The number of galaxies in the sample. Col.(6): Major range of redshift cz of the sample. Col.(7): Major range of FIR luminosity of the sample.

[a]Higher CO luminosity at farther intermediate redshift and mostly mergers or interacting galaxies.

[b]Shallower sample.

[c]Shallower sample in the Southern sky.

[d]Lower cz sample in cluster of galaxies.

[e]Deeper sample with isolated and normal morphology.

cated as a reference by the solid thick line and the solid thin line, respectively. The former is a distance-limited sample, whereas the latter is a flux-limited sample, the flux-limited sample shows a larger SFE. $L_{\rm FIR}/L'_{\rm CO}$ for giant molecular clouds (GMCs) in the Milky Way is distributed between the two dotted lines (Solomon et al. 1987; Mooney, Solomon 1988). Most of the galaxies in the samples have larger values of $L_{\rm FIR}/L'_{\rm CO}$ than that of the GMCs. As Solomon and Sage (1988) and Solomon et al. (1992) indicated, $L_{\rm FIR}/L'_{\rm CO}$ for LIGs is not constant, but increases with the CO luminosity, as shown in figure 4. We fitted all of the samples by a power law, and obtained a relation between the FIR and CO luminosities, given by

$$\log L_{\rm FIR} = 1.41 \log L'_{\rm CO} - 1.60 \quad \text{(all samples)}. \qquad (8)$$

Thus, all of the samples which we examined in this work have a systematically larger SFE than the nearby normal spirals. The IRAM sample shows a remarkably higher SFE, whereas the NRAO-L sample is not far from that of GMCs. Other samples are distributed between them uniformly. Plots of the CO against the FIR luminosities for individual samples are shown in figure 5.

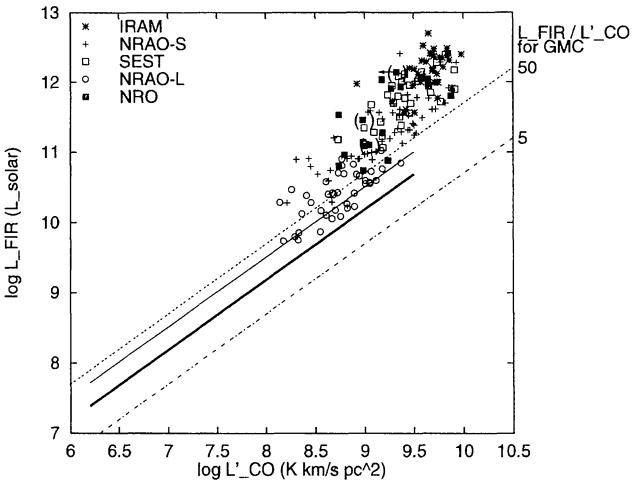

Fig. 4. Diagram of the CO and FIR luminosities. The symbols are the same as in figure 2. The solid thick line indicates the average of 65 nearby spiral galaxies as a distance-limited sample presented by Sage (1993), and the solid thin line indicates the average of 93 nearby spiral galaxies as a flux-limited sample presented by Solomon and Sage (1988); the dispersion is about order of 1. The symbol in parentheses denotes marginal detection, and the symbol with an arrow denotes upper/lower limit. The dotted lines represent the range of $L_{\rm FIR}/L'_{\rm CO}$ seen in giant molecular clouds in the Milky Way ($5 \leq L_{\rm FIR}/L'_{\rm CO} \leq 50$).

3.3. *Gas and Dust Properties*

As indicated in equation (7), the dust mass in galaxies is generally estimated using the IRAS flux at 60 and 100 μm, adopting a single-temperature dust model. However, this estimation overlooks the cold-dust (10–20 K) radiation, because the radiation of cold dust is dominant at $\lambda > 100$ μm, and thus the gas-to-dust ratio is overestimated. The gas-to-dust ratio derived from the IRAS flux for nearby spiral galaxies is typically ~ 570 (Young et al. 1986; Young et al. 1989; Stark et al. 1986). On the other hand, the galactic local gas-to-dust ratio is derived from the gas-column density and the color excess of nearby stars, and therefore should be close to the real gas-to-dust ratio of 100–150 (e.g., Spitzer 1978; Bohlin et al.

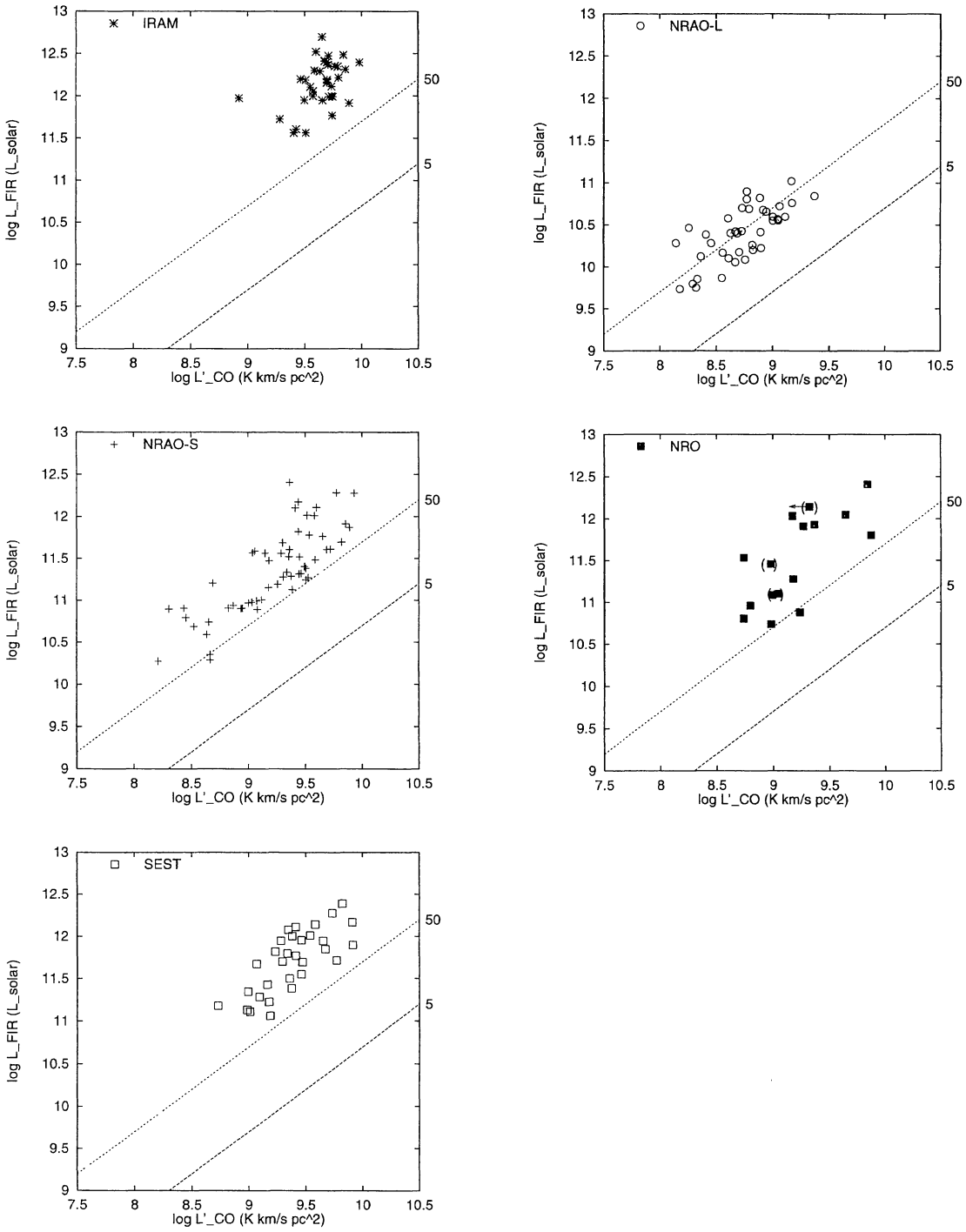

Fig. 5. Diagrams of CO and FIR luminosities for each sample. Dotted lines represent the ratio of $L_{\rm FIR}/L'_{\rm CO}$ of 5 and 50.

1978). It has been suggested that the discrepancy of the gas-to-dust ratio can be explained by two dust components, namely warm and cold dust. The two-component dust model, which consists of cold (10–20 K) dust associated with quiescent molecular clouds and warm (30–60 K) dust associated with star-forming regions, is considered (e.g., de Jong, Brink 1987). For nearby spiral galaxies the discrepancy can be explained when the dust consists of 10–20% warm dust and 80–90% cold dust (Devereux, Young 1990). Figure 6 is a plot of the gas

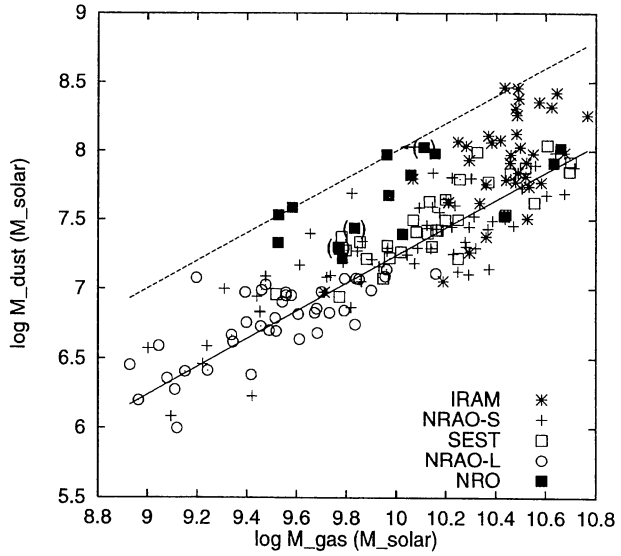

Fig. 6. Diagram of molecular gas mass derived from the CO luminosity and the dust mass derived from the FIR luminosity. The solid line is an observed gas-to-dust ratio ($\sim$ 570) for nearby spiral galaxies using IRAS flux at 100 μm. The broken line represents a typical gas-to-dust ratio of the Galaxy ($\sim$ 100) from observations of nearby stars. The symbol in parentheses denotes marginal detection, and the symbol with an arrow denotes upper/lower limit.

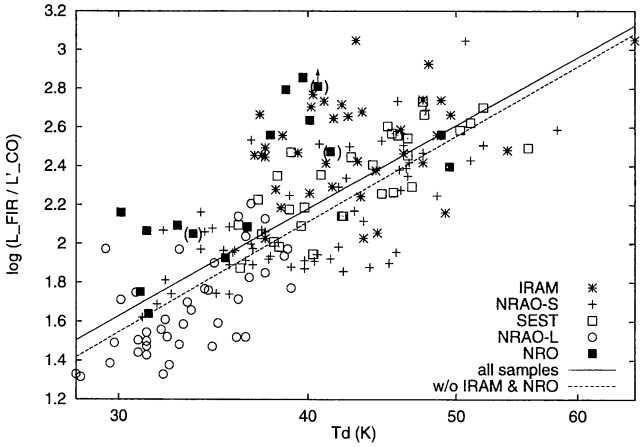

Fig. 7. Diagram of dust temperature and a ratio of FIR-to-CO luminosity. The unit of FIR and CO luminosity are $L_\odot$ and K km s^{-1} pc^2, respectively. The solid and broken line are fitted by a power law for all samples and for the data without the NRO sample and the IRAM sample, respectively. The symbol in parentheses denotes marginal detection, and the symbol with an arrow denotes the upper/lower limit.

mass against the dust mass. Although the NRAO-S, SEST, and NRAO-L samples follow the gas-to-dust ratio of nearby galaxies ($\sim$ 570), the IRAM and NRO samples are distributed between values of nearby galaxies and the Galaxy. This indicates that the warm dust is dominant for the IRAM and NRO samples.

3.4. Warm Dust Fraction

Young et al. (1986) showed that the FIR luminosity of a galaxy depends on both the CO luminosity and the dust temperature. As shown in figure 7, $L_{\rm FIR}/L'_{\rm CO}$ increases with the dust temperature. The IRAM sample and the NRO sample have larger values of $L_{\rm FIR}/L'_{\rm CO}$ at any dust temperature compared to the other samples. We fitted the data in figure 7 by a power law;

$$L_{\rm FIR}/L'_{\rm CO} \propto {T_{\rm d}}^{4.42} \quad \text{(all samples)}, \tag{9}$$

$$L_{\rm FIR}/L'_{\rm CO} \propto {T_{\rm d}}^{4.54} \quad \text{(without IRAM and NRO samples)}. \tag{10}$$

As discussed in the previous subsection, dust in galaxies consists of two components. However, here we assume simply one dust component, whose radiation is dominant in the FIR. Thus, the FIR luminosity is described by

$$L_{\rm FIR} \propto M_{\rm dust} T_{\rm d}^{4+n}, \tag{11}$$

where n is the index of the dust-emissivity law, λ^{-n}. The CO luminosity, $L'_{\rm CO}$, is proportional to gas mass, $M_{\rm gas}$, and $L_{\rm FIR}/L'_{\rm CO}$ is described as

$$L_{\rm FIR}/L'_{\rm CO} \propto \frac{1}{f} T_{\rm d}^{4+n}, \tag{12}$$

where f is the gas-to-dust ratio. The power of the emissivity law is not well established, and is usually adopted as $n = 1$. Therefore, in estimating the dust mass and comparing the results with previous work, we used an emissivity law of $n = 1$. In figure 7, the values of $L_{\rm FIR}/L'_{\rm CO}$ for galaxies in the IRAM and NRO samples are high. It is recognized as being due to the fact that the gas-to-dust ratio for these samples is smaller than that for the other samples. This is consistent with the dominant warm dust in the two-component dust model discussed in the previous subsection.

4. Discussion

4.1. CO Beam Coverage

Smaller gas-to-dust ratios for the NRO and IRAM samples may be induced by missing CO flux due to a smaller beam size. CO observations were performed by single-dish telescopes and pointed at the centers of the target galaxies. Assuming a cosmological model of $h_0 = 0.75$ and $q_0 = 0.5$, the linear scale size of the ^{12}CO (J = 1–0) beam (HPBW) of the telescope along

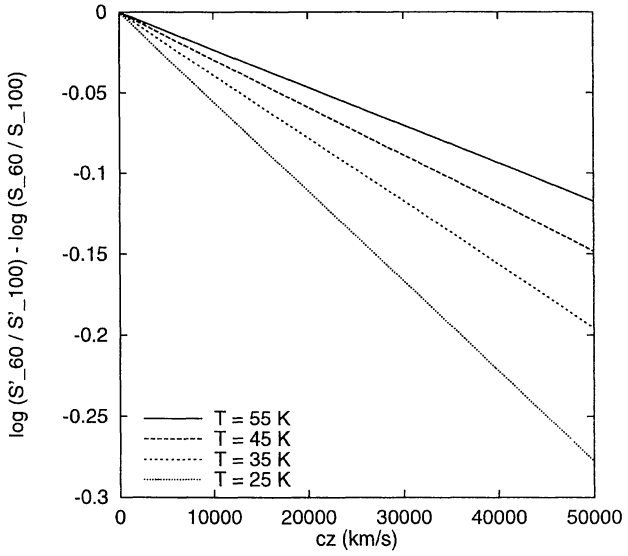

Fig. 8. Residual of IRAS flux ratio of 60 μm to 100 μm (S'_{60}/S'_{100}) to which K-correction is applied, to observed flux ratio (S_{60}/S_{100}). The ordinate is $\log(S'_{60}/S'_{100}) - \log(S_{60}/S_{100})$. Here, we assumed the thermal spectral energy distribution and the emissivity law, $S_\nu \propto \lambda^{-1}$. The lines represent different cases of the dust temperature.

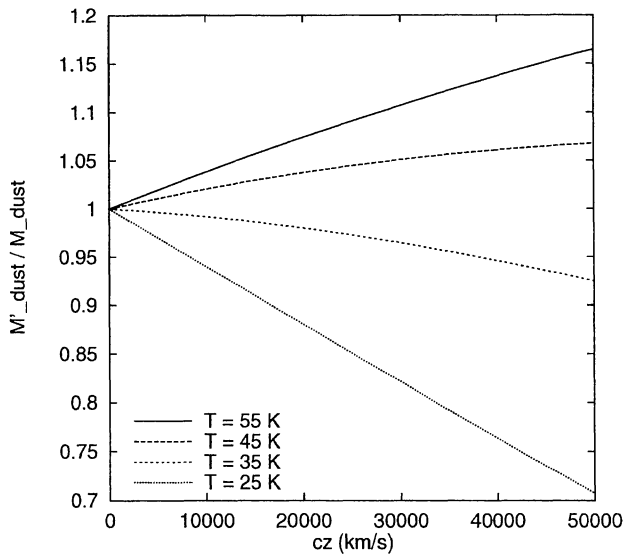

Fig. 9. Ratio of the dust mass to which a K-correction is applied ($M'_{\rm dust}$) to that without a K-correction ($M_{\rm dust}$) along redshift cz, where the thermal spectral energy distribution and the emissivity law, $S_\nu \propto \lambda^{-1}$, are assumed. The lines represent different cases of the dust temperature.

the redshift against angular size is denoted by

$$D(\mathrm{kpc}) = 4.0 \times 10^2\ \theta('')\ \frac{(1+z)^{1/2}-1}{(1+z)^{3/2}}. \qquad (13)$$

The beam sizes of the samples are HPBW = 55″ for the NRAO 12-m telescope, 44″ for the SEST 15-m telescope, 30″ for the IRAM 30-m telescope, and 15″ for the NRO 45-m telescope. Even for the NRO sample, which has the smallest beam, the linear scale size at $cz > 10000$ km s^{-1} is greater than $\sim$ 10 kpc, which should cover the whole extent of the CO-emitting disk of the galaxies.

4.2. IRAS K-Correction

In estimating the dust properties we used the observed IRAS flux densities without any K-correction. We here discuss the effects of a K-correction. Assuming a thermal spectral energy distribution and an emissivity law of $S_\nu \propto \lambda^{-1}$, we estimate the effect of a K-correction on the IRAS flux ratio at 60 μm to 100 μm and on the dust mass. The dust temperature, dust mass, and gas-to-dust ratio are derived from the flux densities at 60 μm and 100 μm. Figure 8 shows a residual of the IRAS flux ratio of 60 μm to 100 μm to which a K-correction is applied (S'_{60}/S'_{100}) to the observed flux ratio without any K-correction (S_{60}/S_{100}). Here the flux densities to which K-correction is applied are denoted by S'_{60} and S'_{100}. The residual for galaxies at a redshift cz of 30000 km s^{-1} with a dust temperature of 40 K is estimated to be -0.1. Adopting this result, the effect of a K-correction is found to be not significant for discussing the galaxy types in figure 10. Figure 9 shows the dust mass ratio to which a K-correction is applied to the observed dust mass without a K-correction. The effect of a K-correction for most of the galaxies used in this study is within 10% of the ratio.

5. Summary

1. We have performed long-integration ^{12}CO (J = 1–0) observations for late-type galaxies at intermediate redshifts $cz \sim$ 10000–50000 km s^{-1} using the NRO 45-m telescope, and have obtained CO line profiles from 16 galaxies with isolated and normal aspects. We compared the observed NRO sample with other CO observations of IRAS galaxies at intermediate redshift, [i.e., Solomon et al. 1997 (IRAM sample); Sanders et al. 1991 (NRAO-S sample); Mirabel et al. 1990 (SEST sample); Lavezzi, Dickey 1998 (NRAO-L sample)], and found that the NRO sample represents the deepest CO observations at intermediate redshifts.

2. We compared the samples in terms of the molecular gas and dust masses. The gas-to-dust ratio for the NRAO-S, SEST, and NRAO-L samples are equivalent to the values found in nearby spirals. On the other hand, the gas-to-dust ratio for the IRAM and NRO samples is

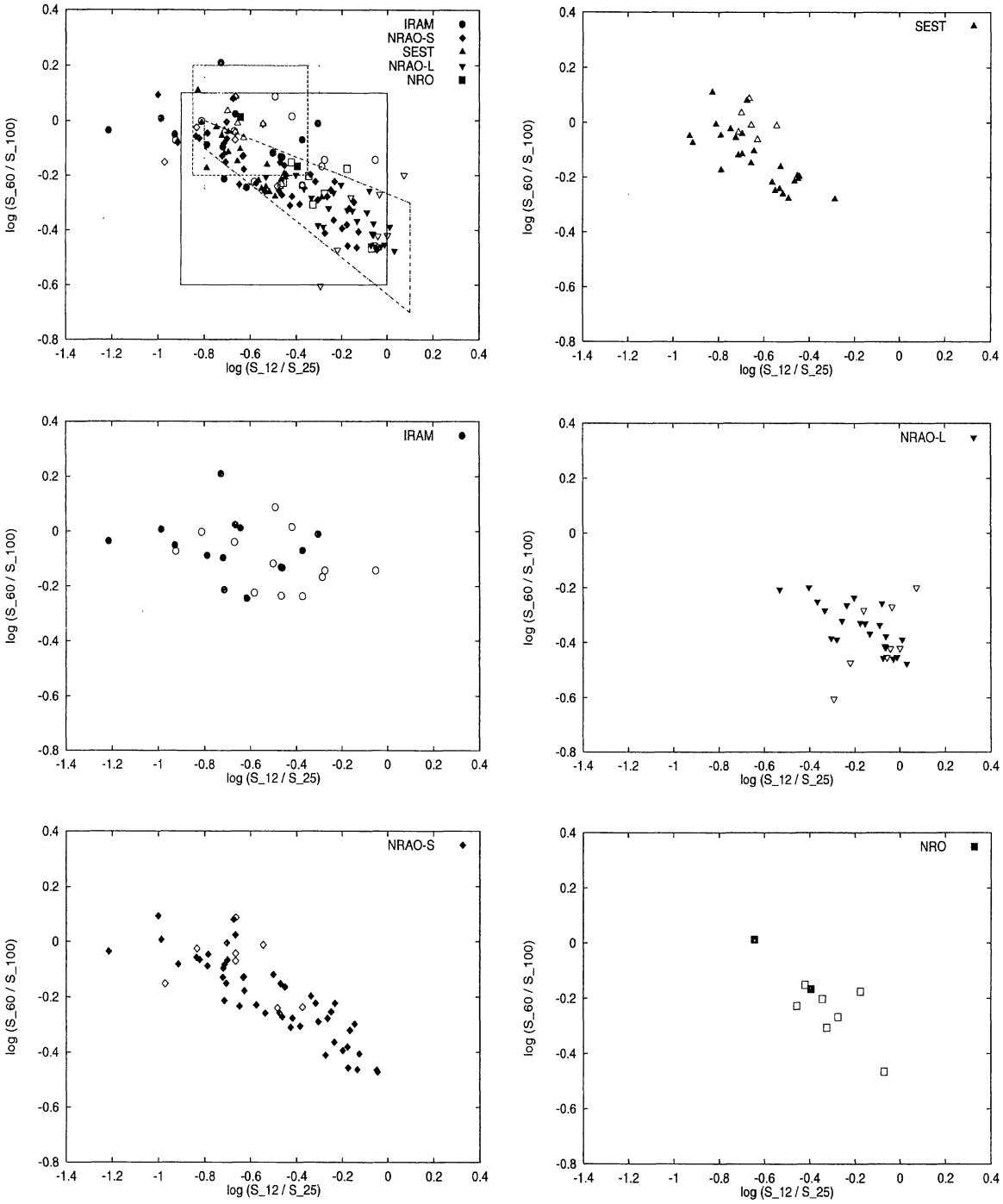

Fig. 10a. IRAS color–color diagrams of the flux densities at 12 μm to 25 μm against 60 μm to 100 μm. All of the samples are shown in the top-left panel, which is overlaid with the IRAM sample (middle-left panel), the NRAO-S sample (bottom-left), the SEST sample (top-right), the NRAO-L sample (middle-right) and the NRO sample (bottom-right). The filled symbols represent fixed values at all of the IRAS bands. The open symbols represent that the 12 μm flux is given as an upper limit; therefore, the real values should be put leftward. The dot-and-broken quadrangle box represents the distribution of the normal and non-IR luminous galaxies with the morphology of Sdm–Im given by Sauvage and Thuan (1994). The distributions of quiescent spiral galaxies, starburst galaxies, and Seyfert galaxies given by Rowan-Robinson and Crawford (1989) are represented by the solid box, broken box, and dotted box, respectively.

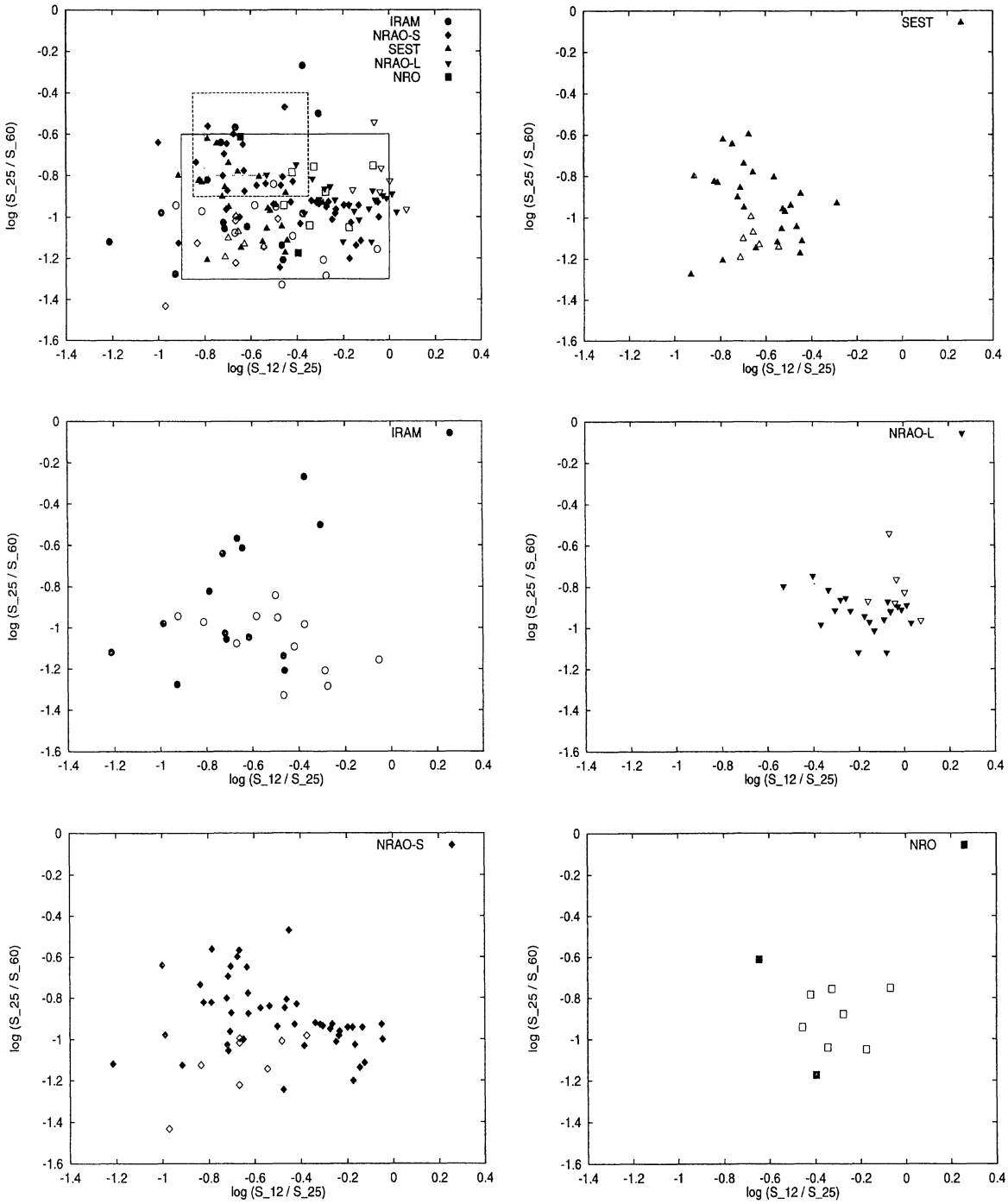

Fig. 10b. IRAS color–color diagrams of 12 μm to 25 μm against 25 μm to 60 μm. The solid box, broken box, and dotted box represent the distribution of quiescent spiral galaxies, starburst galaxies, and Seyfert galaxies, respectively.

smaller than that for the other samples, and is close to the local gas-to-dust ratio of the Galaxy ($\sim$ 100–150), which is derived from gas column density and color excess of nearby stars; it is thus close to real gas-to-dust ratio. The method to estimate dust mass using IRAS flux at 100 μm overlooks cold dust, and the gas-to-dust ratio tends to be overestimated. For nearby spiral galaxies the gas-to-dust ratio is typically 570, which suggests that the dust components consist of a majority of cold dust and a minority of warm dust. This discrepancy can be

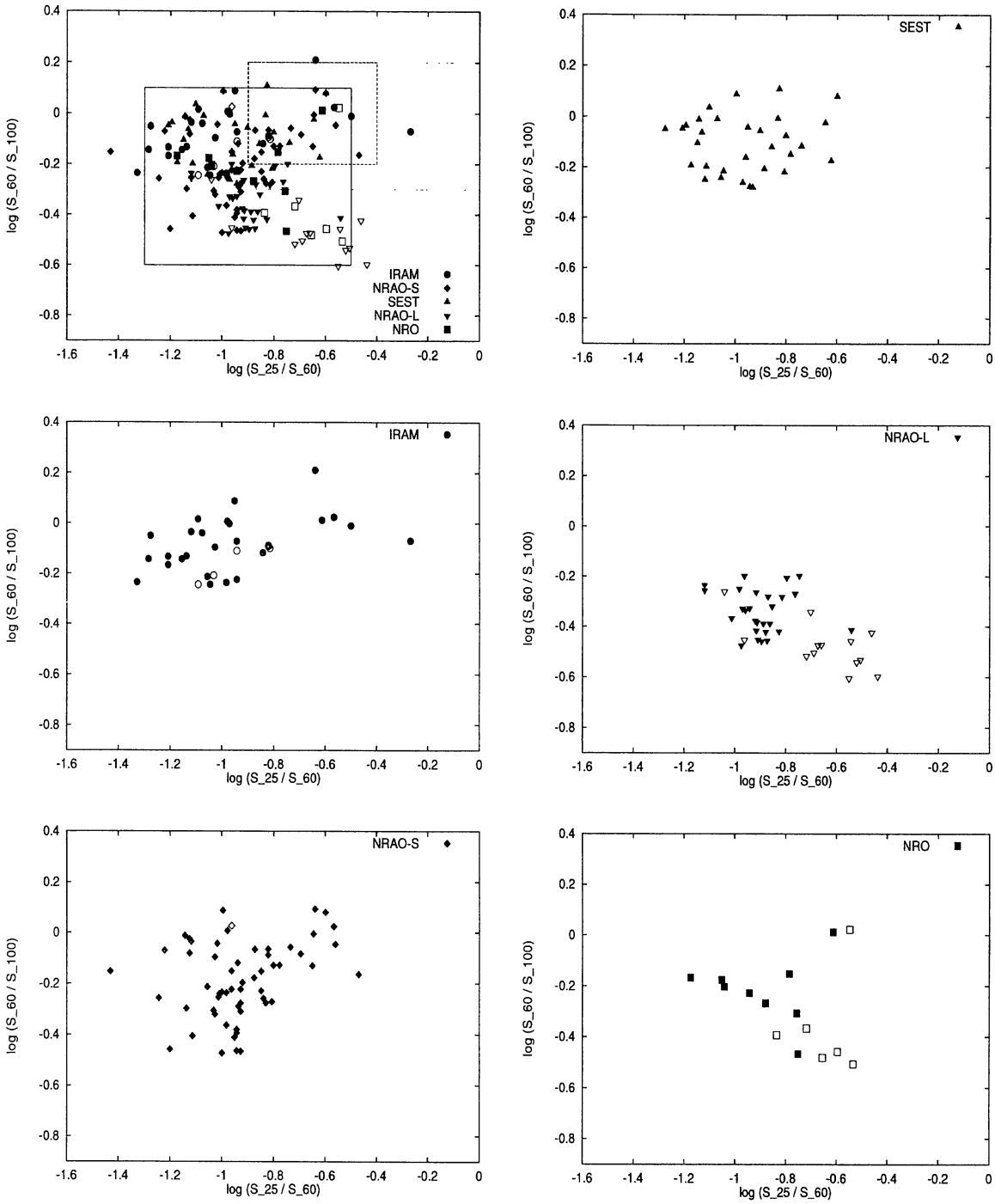

Fig. 10c. IRAS color–color diagrams of 25 μm to 60 μm against 60 μm to 100 μm. Boxes represent the same as the previous figures.

explained if the dust component of the IRAM and NRO samples is mostly warm dust.

3. We compared the samples in terms of IRAS color–color diagrams and galactic nuclear activity, and found that there is no clear peculiarity for the NRO sample. Although the NRO and IRAM samples show a feature of dominant warm dust, the IRAM sample, which consists of mostly mergers or interacting galaxies, shows evidence of very active star-formation, whereas the NRO sample shows moderate star-formation. Thus properties of the

NRO sample are distributed between the IRAM sample and the other samples.

We acknowledge the work of CO-line observations for galaxies at intermediate redshift by Solomon et al., Sanders et al., Mirabel et al., and Lavezzi and Dickey. This research also acknowledges the NASA/IPAC Extragalactic Database to make use of the IRAS data. The authors, Y.T. and M.H., acknowledge financial support by the Research Fellowships of the Japan Society for the Promotion of Science for Young Scientists.

Appendix 1. IRAS Color–Color Diagram

We discussed the FIR luminosity, dust mass, dust temperature, and gas-to-dust ratio estimated from the IRAS fluxes at 60 μm and 100 μm based on the assumption of thermal dust emission with an emissivity law of $n = 1$. In order to test this assumption, we plot a color–color diagram at IRAS wavelengths of 12, 25, 60, and 100 μm. Figure 10a shows IRAS color–color diagrams of $\log(S_{12}/S_{25})$ against $\log(S_{60}/S_{100})$. The top left panel is an IRAS color–color diagram for all the samples. Sauvage and Thuan (1994) examined IRAS color–color diagrams for normal and non-IR luminous galaxies, and discussed the dependency of the morphology of galaxies on a color–color diagram. The dot-and-broken quadrangle box in the top-left panel of of figure 10a represents the distribution of the normal and non-IR luminous galaxies with the morphology of Sdm–Im given by Sauvage and Thuan (1994). Rowan-Robinson and Crawford (1989) also examined IRAS color–color diagrams for starburst, Seyfert, and quiescent spiral galaxies. The distributions of these galaxies are shown in figures 10a–c as the solid box (quiescent spirals), the broken box (starburst galaxies), and the dotted box (Seyfert galaxies), respectively. Galaxies whose IRAS fluxes are known at all IRAS bands are denoted by filled symbols. Galaxies whose 12 μm flux is given by an upper limit are denoted by the open symbols. Therefore, the real data point of the open symbols will be put leftward. Parts of the regions of the quiescent, starburst and Seyfert galaxies overlap. Comparing each sample with the results of Sauvage and Thuan (1994) and Rowan-Robinson and Crawford (1989) in figure 10a, it is found that the IRAM sample and the SEST sample data points fall near to the region of Seyfert and starburst galaxies. The NRAO-S sample is distributed within the region of quiescent spiral galaxies, whereas some galaxies in the samples are plotted at the Seyfert and starburst regions. The NRAO-L sample is distributed in the region of quiescent spiral galaxies. Although in the NRO sample there are only two galaxies whose IRAS fluxes are fixed, the real data point of the galaxies denoted by the open squares will be plotted leftward. Therefore, the NRO sample has characteristics similar to quiescent spiral galaxies, as far as the color–color diagram is concerned. Figures 10b and c are IRAS color–color diagrams for colors of $\log(S_{12}/S_{25})$, $\log(S_{25}/S_{60})$, and $\log(S_{60}/S_{100})$. Comparing them, the same trends as in figure 10a are found.

Appendix 2. Galactic Active Phenomena

It has recently been recognized that the majority of galaxies, even normal galaxies, have a supermassive black hole including the Milky Way (e.g., van der Marel 1998, and references therein), which is suggestive that they have experienced galactic active phenomena, such as starburst, active galactic nuclei (AGN), or powerful radio emission (e.g., Ho et al. 1995) due to supermassive black holes at the galactic center to galaxy interactions. Seyfert and starburst galaxies, whose CO line has been detected, have been discussed in terms of the CO and FIR luminosities (e.g., Mazzarella et al. 1993; Sanders, Mirabel 1996; Rigopoulou et al. 1997). A correlation between the CO and FIR luminosities for Seyfert and starburst galaxies shows the same trend as for LIGs, and is indistinguishable from them (Heckman et al. 1989; Rigopoulou et al. 1997), and also type 1 and type 2 Seyferts show no difference. This suggests that FIR emission in Seyfert and starburst galaxies is responsible for the similar origin (i.e., dust re-radiation of starlight) of ULIGs and normal galaxies. Furthermore, a comparison of the luminosity ratio of FIR to CO, $L_{\rm FIR}/L'_{\rm CO}$, with the dust temperature, $T_{\rm d}$, also shows the same trend as ULIGs and normal galaxies, suggesting that the FIR emission is thermal in origin. Mazzarella et al. (1993) examined the CO and FIR properties of powerful radio galaxies whose CO emission had been detected, and also found the same trend between the CO and FIR luminosities as ULIGs and normal galaxies, whereas non-thermal radio power showed a large excess compared to those objects. This suggests that the origin of powerful radio galaxies may be closely related to the genesis of dust-enshrouded quasar and classical UV-excess quasars through the merging of gas rich disk galaxies (e.g., Sanders et al. 1988a; 1988b). This trend is also clearly found in an examination by Sanders and Mirabel (1996).

In order to discuss the galactic activity for the NRO sample, we compared the CO and FIR properties of nearby Seyfert, starburst, and powerful radio galaxies with the NRO sample and the ULIGs in figures 11 and 12. The nearby CO data references from the literature are as follows: Seyfert galaxies (Heckman et al. 1989), starburst galaxies (Jackson et al. 1989), and powerful radio galaxies which have been detected in the CO-line (Mazzarella et al. 1993). Figure 12 shows the CO and FIR luminosities for the nearby active galaxies compared to the galaxies at intermediate redshift. Figure 12 shows that the excess of $L_{\rm FIR}/L'_{\rm CO}$ for the NRO sample is not directly related

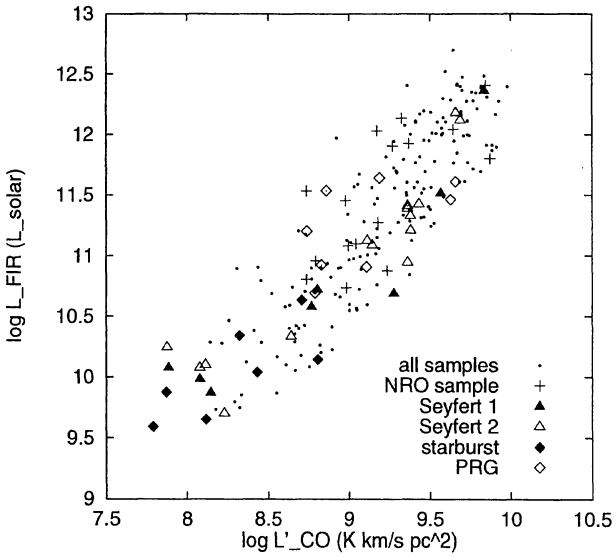

Fig. 11. Comparison of Seyfert, starburst, and powerful radio galaxies with NRO sample and the other samples plotted in figure 4 in terms of the CO and FIR luminosities. Type 1 Seyfert (filled triangles) and type 2 Seyfert (open triangles) are referred to from Heckman et al. (1989), starburst galaxies (filled diamonds) are referred to from Jackson et al. (1989), and powerful radio galaxies (open diamonds) are referred to from Mazzarella et al. (1993). The NRO sample and the other samples are denoted by crosses and small dots, respectively.

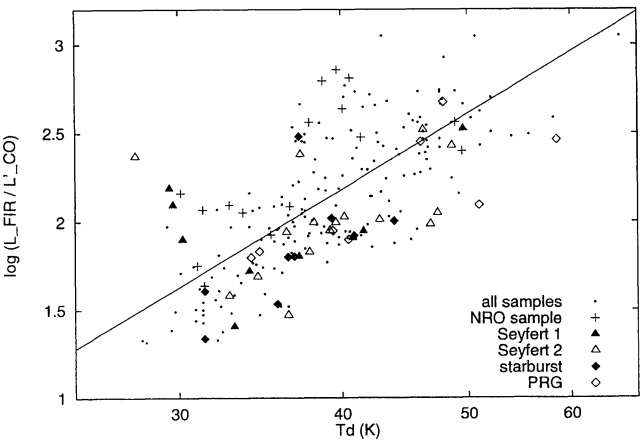

Fig. 12. Comparison of Seyfert, starburst and powerful radio galaxies with the NRO sample and the other samples plotted in figure 7 in terms of the CO-to-FIR luminosity ratio ($L_{\rm FIR}/L'_{\rm CO}$) and the dust temperature ($T_{\rm d}$). The symbols and the references are the same as figure 11. The solid line is the regression line fitted by a power law for all the samples used in figure 7.

to the galactic activity. The active galaxies are indistinguishable from the galaxies at intermediate redshift.

References

Allen C.W. 1973, in Astrophysical Quantities, 3rd ed (Athlone Press, London)

Bohlin R.C., Savage B.D., Drake J.F. 1978, ApJ 224, 132

de Jong T., Brink K. 1987, sfig conf, 323

de Vaucouleurs G., de Vaucouleurs A., Corwin H.G.Jr, Buta R.J., Parurel G., Fouqué P. 1991, Third Reference Catalog of Bright Galaxies (Springer-Verlag, New York) (RC3)

Devereux N.A., Young J.S. 1990, ApJ 359, 42

Downes D., Solomon P.M., Radford S.J.E. 1993, ApJ 414, L13

Elfhag T., Booth R.S., Höglund B., Johansson L.E.B., Sandqvist A. 1996, A&AS 115, 439

Fisher K.B., Huchra J.P., Strauss M.A., Davis M., Yahil A., Schlegel D. 1995, ApJS 100, 69

Heckman T.M., Blitz L., Wilson A.S., Armus L., Miley G.K. 1989, ApJ 342, 735

Hildebrand R.H. 1983, QJRAS 24, 267

Ho L.C., Filippenko A.V., Sargent W.L. 1995, ApJS 98, 477

Jackson J.M., Snell R.L., Ho P.T.P., Barrett A.H. 1989, ApJ 337, 680

Lavezzi T.E., Dickey J.M. 1998, AJ 116, 2672 [NRAO-L sample]

Mazzarella J.M., Graham J.R., Sanders D.B., Djorgovski S. 1993, ApJ 409, 170

Mirabel I.F., Booth R.S., Garay G., Johansson L.E.B., Sanders D.B. 1990, A&A 236, 327 [SEST sample]

Mooney T.J., Solomon P.M. 1988, ApJ 334, L51

Rickard L.J., Harvey P.M. 1984, AJ 89, 1520

Rigopoulou D., Papadakis I., Lawrence A., Ward M. 1997, A&A 327, 493

Rowan-Robinson M., Crawford J. 1989, MNRAS 238, 523

Sage L.J. 1993, A&A 272, 123

Sanders D.B., Mirabel I.F. 1985, ApJ 298, L31

Sanders D.B., Mirabel I.F. 1996, ARA&A 34, 749

Sanders D.B., Scoville N.Z., Soifer B.T. 1991, ApJ 370, 158 [NRAO-S sample]

Sanders D.B., Soifer B.T., Elias J.H., Madore B.F., Matthews K., Neugebauer G., Scoville N.Z. 1988a, ApJ 325, 74

Sanders D.B., Soifer B.T., Elias J.H., Neugebauer G., Matthews K. 1988b, ApJ 328, L35

Sauvage M., Thuan T.X. 1994, ApJ 429, 153

Soifer B.T., Rowan-Robinson M., Houck J.R., de Jong T., Neugebauer G., Aumann H.H., Beichman C.A., Boggess N. et al. 1984, ApJ 278, L71

Solomon P.M., Barrett J.W. 1991, in Dynamics of Galaxies and Their Molecular Clouds Distributions, ed F. Combes, F. Casoli (Kluwer, Dordrecht) p235

Solomon P.M., Downes D., Radford S.J.E., Barrett J.W. 1997, ApJ 478, 144 [IRAM sample]

Solomon P.M., Radford S.J.E., Downes D. 1992, Nature 356, 318

Solomon P.M., Rivolo A.R. 1989, ApJ 339, 919

Solomon P.M., Rivolo A.R., Mooney T.J., Barrett J.W., Sage L.J. 1987, in Proc. Star Formation in Galaxies, Pasadena, ed C.J. Lonsdale, S.E. Persson, NASA CP-2466, p37
Solomon P.M., Sage L.J. 1988, ApJ 334, 613
Spitzer L. 1978, Physical processes in the interstellar medium (Wiley-Interscience, New York)
Stark A.A., Knapp G.R., Bally J., Wilson R.W., Penzias A.A., Rowe H.E. 1986, ApJ 310, 660
Strauss M.A., Huchra J.P., Davis M., Yahil A., Fisher K.B., Tonry J. 1992, ApJS 83, 29
Strong A.W., Bloemen J.B.G.M., Dame T.M., Grenier I.A., Hermsen W., Lebrun F., Nyman L.A., Pollock A.M.T. et al. 1988, A&A 207, 1
Tinney C.G., Scoville N.Z., Sanders D.B., Soifer B.T. 1990, ApJ 362, 473
Tutui Y., Sofue Y. 1997, A&A 326, 915
van der Marel R.P. 1998, in Galaxy Interaction at Low and High Redshift, ed J.E. Barnes, D.B. Sanders (Kluwer, Dordrecht) p333
Young J.S., Kenney J., Lord S.D., Schloerb F.P. 1984, ApJ 287, L65
Young J.S., Schloerb F.P., Kenney J.D., Lord S.D. 1986, ApJ 304, 443
Young J.S., Xie S., Kenney J.D.P., Rice W.L. 1989, ApJS 70, 699
Young J.S., Xie S., Tacconi L., Knezek P., Viscuso P., Tacconi-Garman L., Scoville N., Schneider S. et al. 1995, ApJS 98, 219